Global Nonhydrostatic Modeling Using Voronoi Meshes

William Skamarock, Joseph Klemp,
Michael Duda, Laura Fowler and Sang-Hun Park

National Center for Atmospheric Research
Boulder, Colorado, USA
skamaroc@ucar.edu

ABSTRACT

We present a brief overview of the numerical methods used in the global nonhydrostatic atmospheric solver in the Model for Prediction Across Scales (MPAS). MPAS-Atmosphere solves the fully compressible nonhydrostatic equations on a horizontally-unstructured centroidal Voronoi mesh using finite volume techniques. The numerics are, in many aspects, an extension of modeling techniques embodied in existing regional nonhydrostatic cloud and mesoscale models. This overview focusses on the Voronoi mesh extensions to these techniques and on preliminary model results validating the new formulation.

1 Introduction

The Model for Prediction Across Scales (MPAS) is composed of geophysical fluid-flow solvers for the atmosphere and ocean; the atmospheric component (MPAS-A; Skamarock et al, 2012) is being developed by the National Center for Atmospheric Research, the ocean component (MPAS-O; Ringler et al, 2013) is being developed by the Los Alamos National Laboratory under the US Department of Energy, and the shared infrastructure has been jointly developed. In this paper we provide a brief overview of the atmospheric component of MPAS along with some preliminary results demonstrating its performance.

MPAS-A solves the fully compressible nonhydrostatic equations of motion utilizing a fully-unstructured spherical centroidal Voronoi tessellation (SCVT; Ringler et al, 2008; Du et al, 2003) in its horizontal discretization. An example mesh, depicted in figure 1, illustrates two important features of the mesh. First, the mesh permits a quasi-uniform discretization of the sphere and it does not suffer from the pole problems inherent with the use of latitude-longitude meshes, including the numerical accuracy and computational-efficiency issues. Second, the unstructured mesh allows for variable horizontal resolution that is highly flexible. This flexibility makes it possible to produce high-resolution regional NWP forecasts, and regional climate simulations, directly within a global model without the lateral boundary-condition problems found in traditional one-way and two-way nested approaches. The SCVTs and their construction are outlined in section 2.

Recognizing that divergent modes (convection, gravity waves) are the most important features at the margins of our mesh resolution in meso- and cloud-scale simulations, we utilize a C-grid staggering of the prognostic variables in order to increase the accuracy of the pressure gradient and velocity divergence operators relative to unstaggered-mesh models. The C-grid staggering of the prognostic variables defines the prognostic horizontal and vertical velocities as those velocities normal to the Voronoi cell faces, whereas all other quantities are defined at cell centers (or, formally, as cell averages). Additionally, the horizontal momentum equation uses a vector invariant formulation whereby the nonlinear momentum transport is recast as a gradient of kinetic energy and an additional nonlinear Coriolis term (Ringler et al 2009). This aspect of the formulation removes the difficulties associated with discretizing the nonlinear vector momentum transport on the unstructured mesh. Critical aspects of the discretization of the dry
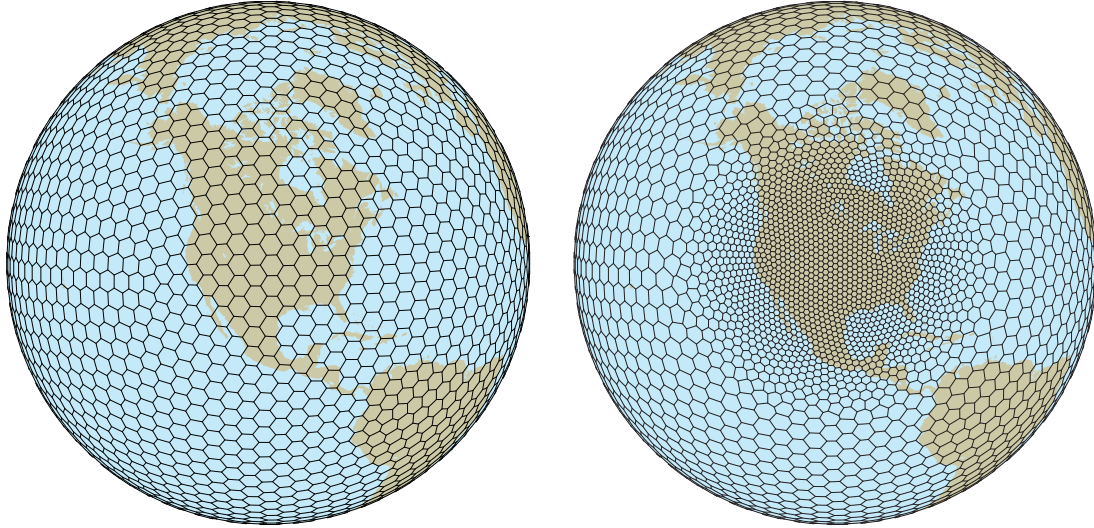
Figure 1: Quasi-uniform resolution Voronoi mesh (left) and variable resolution mesh (right).

solver associated with the C-grid Voronoi mesh are considered in section 3.

The fully compressible nonhydrostatic equations are cast in flux form in which potential temperature and scalar mixing ratios are coupled with density (Klemp et al, 2007). This formulation allows for a straightforward discretization of the flux divergence on the Voronoi mesh that guarantees exact (to machine roundoff) conservation of air mass, scalar mass, and entropy. A third-order accurate transport scheme, derived as an extension of a scheme used on orthogonal rectangular meshes, is used on the Voronoi mesh in MPAS for both the atmosphere and ocean solvers. We discuss the equations and the temporal and spatial discretization of the scalar transport equations in Section 4.

While existing computational capabilities do not permit frequent production and use of global nonhydrostatic scale simulations, exploratory global simulations with mesh spacings of a few kilometers are no longer unique. In section 5 we conclude by presenting some examples, from global 3km simulations and coarser-mesh simulations, of fine-scale structure in convection and mountain waves. The structures are consistent with those simulated in state of the art limited area cloud models, and they represent our first step towards validating the capabilities of the global nonhydrostatic MPAS-A solver. In addition, we show kinetic energy spectra indicating that effective resolution is similar to that of the regional models, supporting our tuning of the model filters.

2   Spherical Centroidal Voronoi Tesselations

The unstructured meshes used by the ocean and atmosphere solvers in MPAS are known as spherical centroidal Voronoi tesselations (SCVTs). Ringler et al (2008) describe the meshes and their properties and methods for generating them for climate system model applications. Du et al (2003) presents a more general description of the properties of these meshes. We have chosen to use these meshes because they allow both uniform and variable-resolution tiling of the sphere, and because they do not suffer from a number of problems encountered with the use of the commonly used latitude-longitude mesh, including the strong anisotropy of latitude-longitude mesh cells near the poles, the need for polar filters, and issues associated with parallelization of the latitude-longitude mesh numerics.

Figure 2 depicts a portion of a Voronoi mesh. The key properties of the SCVT are:
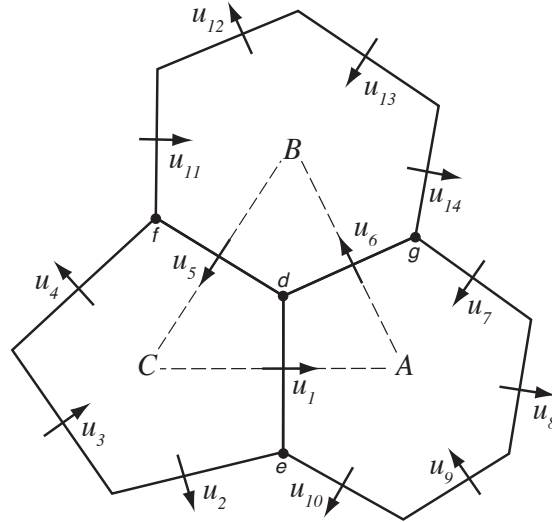
Figure 2: Voronoi mesh cells with C-grid staggered velocities. Adapted from Skamarock et al (2012) figure 1.

1. The cell centers (*A*, *B*, and *C* in figure 2) are the cell centers of mass.

2. The lines connecting the cell centers (*AB*, *BC*, *CA* in figure 2) are perpendicular to the cell edges (*de*, *df* and *dg* in figure 2) at their intersection points. These lines are great-circle arcs on the sphere.

3. The lines connecting the cell centers (*AB*, *BC*, *CA* in figure 2) are bisected by the cell edges (*de*, *df* and *dg* in figure 2). Note that the cell edges, however, are not bisected by the lines connecting the cell centers.

These properties play an important role on the accuracy and robustness of the MPAS solvers as will be discussed in section 3 and 4.

The *dual* of the SCVT is the triangular mesh constructed by connecting the cell centers (e.g. *ABC* in figure 2), and it is called the *Delaunay triangulation*. The vertices of the polygons in the SCVT are the cell centers in the Delaunay triangulation, and likewise the vertices of the polygons (triangles) in the Delaunay triangulation are the cell centers in the SCVT. The mesh given by the Delaunay triangulation is made up entirely of triangles, in contrast to the indeterminate number of cell edges for the cells in the SCVT. The role of the Delaunay triangulation in the MPAS numerics will be discussed in section 3.

SCVTs are generated using an iterative procedure known as Lloyd's method (Lloyd, 1982; Ringler et al, 2008). Starting with a set of randomly distributed generator points (the cell centers), (i) the Voronoi diagram (mesh) is constructed, (ii) the cell centers-of mass are determined, and (iii) convergence criteria are computed. Typically the convergence criteria is some norm of the distance between the generator points and the cell centers of mass. If convergence has not been reached, the generator points are replaced with the cell centers of mass and steps (i)-(iii) are repeated. This iterative procedure converges, albeit slowly. We note here that the connectivity of the generator points, determined during the construction of the Voronoi diagram, can change at each iteration, and the iterations can lead to a significant redistribution of the points.

In Lloyd's method, the center of mass for a cell can be defined with respect to a arbitrary density function ρ as

$$\mathbf{x} = \frac{\int_V \mathbf{y} \rho(\mathbf{y}) \, d\mathbf{y}}{\int_V \rho(\mathbf{y}) \, d\mathbf{y}},$$

where the integral is over a Voronoi cell. A quasi-uniform mesh is produced for $\rho = 1$, and the cell center spacing h will vary little over the mesh. If a nonuniform density ρ is prescribed, then the cell center spacing h will be

$$\frac{h_{V_i}}{h_{V_j}} \approx \left(\frac{\rho(\mathbf{x}_j)}{\rho(\mathbf{x}_i)} \right)^{1/4}$$

The mesh in Figure 1 features a refinement ratio of 4, and the density function varies by a factor of 256 between the uniform values in the coarse and fine mesh regions. The arbitrary density functions allow us great flexibility, and our experience indicates that solver accuracy depends on the smoothness of the mesh transitions between regions of differing resolution.

On quality meshes (see Ringler et al, 2008), SCVTs on the sphere are composed of convex polygons, primary hexagons but also including pentagons and possibly septagons (the variable-resolution mesh in figure 1 contains all three). For quasi-uniform resolution applications, MPAS uses standard icosahedral meshes (see Lipscomb and Ringler, 2005) that have been converged using Lloyd's method; the connectivity of these quasi-uniform meshes are unchanged from their icosahedral origins.

3 Atmospheric Solver

MPAS-A solves the fully compressible equations of motion are cast in conservative (flux) form as described in Skamarock et al (2012). The terrain-following hybrid vertical coordinate used in MPAS, based on geometric height, is described in Klemp (2011). The vertical coordinate is denoted as ζ and its vertical derivate with respect to height ζ_z. The MPAS prognostic variables are given as

$$(U, V, W, \Theta_m, Q_j) = \tilde{\rho}_d \cdot (u, v, w, \theta_m, q_j),$$

where ρ_d is the density of dry air, $\tilde{\rho}_d = \rho_d / \zeta_z$, q_j represents the mixing ratio of the respective water species, and

$$\theta_m = \theta \left[1 + (R_v / R_d) q_v \right]$$

is a modified moist potential temperature with q_v representing the water vapor mixing ratio. The velocities (u, v, w) represent two orthogonal horizontal velocities and a vertical velocity radially outward from the center of the earth; the velocities obey the right-hand rule, $\vec{v} = (u\vec{i}, v\vec{j}, w\vec{k})$ where $\vec{i} \times \vec{j} = \vec{k}$. $\Omega = \mathbf{V} \cdot \nabla \zeta$ is the component of the mass flux normal to the coordinates surfaces in the transformed coordinate, where $\mathbf{V} = (U, V, W)$. Defining the additional metric terms $z_H = -(\zeta_x, \zeta_y)/\zeta_z$, the full equation set can be expressed as

$$\frac{\partial \mathbf{V}_H}{\partial t} = -\frac{\rho_d}{\rho_m} \left[\nabla_\zeta \left(\frac{p}{\zeta_z} \right) - \frac{\partial z_H p}{\partial \zeta} \right] - \eta \, \mathbf{k} \times \mathbf{V}_H$$

$$- \mathbf{v}_H \nabla_\zeta \cdot \mathbf{V} - \frac{\partial \Omega \mathbf{v}_H}{\partial \zeta} - \rho_d \nabla_\zeta K - eW \cos \alpha_r - \frac{uW}{r_e} + \mathbf{F}_{V_H}, \tag{1}$$

$$\frac{\partial W}{\partial t} = -\frac{\rho_d}{\rho_m} \left[\frac{\partial p}{\partial \zeta} + g \tilde{\rho}_m \right] - \left(\nabla \cdot \mathbf{v} W \right)_\zeta$$

$$+ \frac{uU + vV}{r_e} + e \left(U \cos \alpha_r - V \sin \alpha_r \right) + F_W, \tag{2}$$

$$\frac{\partial \Theta_m}{\partial t} = -\left(\nabla \cdot \mathbf{V} \theta_m \right)_\zeta + F_{\Theta_m}, \tag{3}$$

$$\frac{\partial \tilde{\rho}_d}{\partial t} = -\left(\nabla \cdot \mathbf{V} \right)_\zeta, \tag{4}$$

$$\frac{\partial Q_j}{\partial t} = -\left(\nabla \cdot \mathbf{V} q_j \right)_\zeta + F_{Q_j}. \tag{5}$$

Pressure is obtained diagnostically from the equation of state,

$$p = p_0 \left(\frac{R_d \zeta_z \Theta_m}{p_0} \right)^\gamma,$$

with $\gamma = c_p/c_v$. Here, ρ_m is the density of moist air,

$$\frac{\rho_m}{\rho_d} = 1 + q_v + q_c + q_r + \dots,$$

where q_v, q_c, q_r are mixing ratios of vapor, cloud water, rain water, etc. In (1), $\eta = \boldsymbol{k} \cdot \boldsymbol{\nabla} \times \boldsymbol{v}_H + f$ is the absolute vertical vorticity, and $K = |\boldsymbol{v}_H|^2/2$ is the horizontal kinetic energy. In the curvature and Coriolis terms in (1) and (2), $f = 2\Omega_e \sin \psi$, $e = 2\Omega_e \cos \psi$, ψ is the latitude, Ω_e is the angular rotation rate of the earth, r_e is the earth radius, and α_r is the rotation angle between the line normal to the horizontal velocity and the meridians. The terms $\boldsymbol{F}_{V_H}$, F_W, F_{Θ_m} and F_{Q_j} represent sources and sinks from physics, sub-grid models and filters. Following the notation of Dutton (1986) we define $(\boldsymbol{\nabla} \cdot \boldsymbol{V}b)_\zeta = \boldsymbol{\nabla}_\zeta \cdot (\boldsymbol{V}_H b) + \partial(\Omega b)/\partial \zeta$ for any scalar b, where $\boldsymbol{\nabla}_\zeta$ refers to the divergence operator along a constant ζ surface and $\boldsymbol{V}_H = (U, V)$.

The MPAS-A integration scheme for (1)-(5) is described in Skamarock et al (2012). A detailed description and analysis of the time-splitting used to accommodate the acoustic modes is described in Klemp et al (2007) and Wicker and Skamarock (2002). In the remainder of this section we outline the important aspects of this scheme that differentiate it from similar schemes implemented on rectangular meshes. However, we first point out that MPAS uses a C-grid discretization on the Voronoi mesh, and this staggering retains the properties present on rectangular-mesh implementations such as the regional model WRF (Skamarock and Klemp, 2008) and the UK Meteorological Office model (Davies et al, 2005). Specifically, the horizontal pressure gradient calculation is fully second-order accurate on the Voronoi mesh because the cell edges bisect the (orthogonal) line connecting the cell centers, and this discrete gradient is twice as accurate as that on an unstaggered mesh because is it computed over a spacing of Δh as opposed to a $2\Delta h$ gradient operator used on an unstaggered (A-grid) mesh. The divergence is second-order accurate for edge-centered velocities. The velocities are not centered on the Voronoi mesh, but for smooth meshes the induced error is small. Importantly, the C-grid does not suffer from a non-zero null space in pressure or velocity, i.e. the pressure gradient and divergence operators see the $2\Delta h$ modes in the pressure and velocity fields; the A-grid does not see these $2\Delta h$ modes.

The prognostic coupled horizontal velocities U are defined as the velocities normal to the cell face at the point where the lines connecting the cell centers are bisected by the cell edges (see figure 2). MPAS uses a vector invariant formulation of the horizontal momentum equation, and the vertical vorticity η and the velocity tangential to the cell face $\boldsymbol{k} \times \boldsymbol{V}_H$ are needed to integrate (1).

Vertical vorticity naturally resides at the cell vertices; it is most compactly computed by integrating the circulation about the dual mesh (Delaunay) cells. The vertex vorticity can then be averaged to the cell face or computed using an upwind interpolation as described in Ringer et al (2009) which provides for dissipation of enstrophy.

The determination of the horizontal velocity tangential to the cell edges lies at the heart of the MPAS formulation. Consider the determination of the velocity perpendicular to u_1 in figure 2. The simplest approach is to use a weighted sum of the nearest neighbor velocities (u_2, u_5, u_6, and u_{10}). This approach produces noisy, unusable solutions (Ničković et al, 2002). The problem is most easily understood by examining the linearized shallow water equations as applied to the Voronoi mesh - a non-stationary geostrophic mode is produced on the Voronoi mesh in place of the stationary geostrophic mode present in the exact solution. Thuburn et al (2009) developed a reconstruction of the tangential velocity that recovered the stationary mode. It consists of a weighted sum of all the prognostic velocities from the edges of the two cells sharing the edge where the tangential velocity reconstruction is required (i.e. u_2 through u_{10} in figure 2). The reconstruction has the important property that the mass divergence

computed on the dual (Delauney) triangulation, using the reconstructed mass fluxes (velocities) normal to the Delaunay cell edges, is the weighted sum of the mass divergences of the three Voronoi cells. Additionally, the mass divergence integrated over the dual (Delaunay) mesh equals the integral over the Voronoi mesh, thus mass is conserved in a consistent manner on both meshes, both locally and globally. The constraint on the mass divergence on the dual (Delaunay) mesh, where the vorticity is defined, is sufficient to recover the stationary geostrophic mode and removes the C-grid icosahedral mesh issues outlined in Ničković et al (2002).

Ringler et al (2009) leverages the reconstruction in Thuburn et al (2009) to produce a potential vorticity (PV) conserving scheme for the shallow water equations that also conserves energy to machine roundoff. Energy conservation is directly tied to the reconstruction of the kinetic energy at the cell centers, where it is used in the kinetic energy gradient operator in (1). Ringler et al (2009) show that a specific weighted sum of the squared prognostic velocities on the cell faces is needed for energy conservation. MPAS-A uses a modification to this kinetic energy reconstruction to resolve issues associated with an instability believed to be related to that described by Hollingsworth (1983). Details are described in Skamarock et al (2012).

PV conservation in the MPAS shallow water equations solver relies on a specific discretization of the nonlinear Coriolis term that has been carried over to the discretization of the MPAS-A horizontal momentum equation (1). We can define the Thuburn et al (2009) tangential velocity reconstruction as

$$v_{e_i} = \sum_{j=1}^{n_{e_i}} w_{e_{i,j}} u_{e_{i,j}}, \tag{6}$$

where the reconstruction is for edge e_i, and the summation is over the edges $e_{i,j}$ contributing to the reconstruction. The discretization of the term $\eta \, \boldsymbol{k} \times \boldsymbol{V}_H$ in (1) that leads to PV conservation can now be expressed as

$$[\eta \, \boldsymbol{k} \times \boldsymbol{V}_H]_{e_i} = \sum_{j=1}^{n_{e_i}} \frac{1}{2} (\eta_{e_i} + \eta_{e_{i,j}}) w_{e_{i,j}} \rho_{e_{i,j}} u_{e_{i,j}}, \tag{7}$$

where density at the cell edge j, $\rho_{e_{i,j}}$, is the average of the two densities in from the cells sharing the edge. Note that the mass flux reconstruction follows (6) but the vorticity in each weighted component is the average of the vorticity at the reconstruction edge and the contributing weighted edge.

4   Transport Scheme

Mass and scalar conservation equations (3), (4) and (5) are cast in conservative form. We use a finite volume (FV) formulation to ensure scalar conservation in the discrete formulation wherein the flux divergence (in this case in 2D) is cast in integral form

$$\frac{\partial (\overline{\rho \psi})_i}{\partial t} = -\frac{1}{A_i} \int_{\Gamma_i} \rho \, \psi \boldsymbol{V} \cdot \boldsymbol{n}_i \, \partial \Gamma.$$

where ψ is a generic scalar and $\overline{\rho \psi}_i$ denotes the average value of $\rho \psi$ over the volume A_i. The 2D integral of the flux divergence over A_i has been recast into an integral over the boundary Γ_i of the boundary-normal flux. The discrete spatial formulation for the Voronoi mesh is

$$\frac{\partial (\overline{\rho \psi_i})}{\partial t} = -\frac{1}{A_i} \sum_{n_{e_i}} d_{e_i} \boldsymbol{F}_{e_i} (\boldsymbol{V}, \psi), \tag{8}$$

where A_i is the area of cell i, d_{e_i} is the length of edge e_i, and the summation is over the edges of cell i. The instantaneous flux $\boldsymbol{F}_{e_i}(\boldsymbol{V}, \psi) = (\boldsymbol{V} \cdot \boldsymbol{n}_{e_i}) \psi$, where $\boldsymbol{n}_{e_i}$ is the outward-directed unit normal. Equation

(8) is still exact - the approximation results from the discretization of the time derivative term and the fluxes.

We use the MPAS-A 3rd-order Runge-Kutta time integration scheme to discretize the time derivative in (8). The spatial discretization of the fluxes $\boldsymbol{F}_{e_i}$ is described in Skamarock and Gassmann (2011), and it is an extension of the 3rd-order scheme described in Hundsdorfer et al (1995). Using a 1D mesh with constant mesh spacing and constant density, the Hundsdorfer et al evaluation of the flux is

$$\boldsymbol{F}(u,\psi)_{i+1/2} = u_{i+1/2}\left[\frac{1}{2}\left(\psi_{i+1}+\psi_i\right) - \frac{1}{12}\left(\delta_x^2\psi_{i+1}+\delta_x^2\psi_i\right) + sign(u)\frac{\beta}{12}\left(\delta_x^2\psi_{i+1}-\delta_x^2\psi_i\right)\right], \quad (9)$$

where the variable ψ is defined at evenly-spaced mesh points i, and the operator $\delta_x^2\psi$ denotes $\psi_{i+1} - 2\psi_i + \psi_{i-1}$. For $\beta = 0$ the formulation (9) results in a 4th-order accurate discretization of the flux divergence in space using (8). Hundsdorfer et al (1995) suggest using $\beta = 1$ which results in a third-order accurate flux-divergence discretization. The addition of the term multiplied by β introduces a 4th-order dissipation proportional to the Courant number $u\Delta t/\Delta x$ in the full scheme. The addition of the dissipation term, while decreasing the overall scheme order and increasing the diffusive character of the scheme, lowers the phase errors in the scheme.

While the 1D flux calculation (9) can easily be applied easily on quadrilateral meshes, (9) cannot be used on the Voronoi mesh; ψ is not constantly spaced along gridlines normal to a given cell edge. For use in MPAS, we replace the flux calculation (9) with

$$F(u,\psi)_{i+1/2} = u_{i+1/2}\left[\frac{1}{2}\left(\psi_{i+1}+\psi_i\right) - \Delta x_e^2\frac{1}{12}\left\{\left(\frac{\partial^2\psi}{\partial x^2}\right)_{i+1}+\left(\frac{\partial^2\psi}{\partial x^2}\right)_i\right\}\right.$$
$$\left. + sign(u)\Delta x_e^2\frac{\beta}{12}\left\{\left(\frac{\partial^2\psi}{\partial x^2}\right)_{i+1}-\left(\frac{\partial^2\psi}{\partial x^2}\right)_i\right\}\right], \quad (10)$$

where Δx_e is the distance between cell centers i and $i+1$ that share edge e, x is the direction normal to edge e, and $u_{i+1/2}$ is the velocity normal to cell edge e and is positive for flow from cell i to cell $i+1$. We replace the operator $\delta_x^2\phi$ in (9) with the second derivative of a least-squares fit polynomial for ψ, taken in the direction normal to the cell edge, multiplied by the square of the distance between the cell centers that share that edge. Equation (10) represents 3rd-order ($\beta \neq 0$) or 4th-order ($\beta = 0$) accurate algorithms for meshes with constant mesh spacing Δx and constant velocity. On the MPAS Voronoi mesh, Skamarock and Gassmann demonstrate 3rd-order convergence for this scheme on the sphere with smooth meshes, and they recommend $\beta = 0.25$ when used with an FCT-based shape-preserving limiter. Details of the scheme and its implementation on the Voronoi mesh are given in Skamarock and Gassmann (2011).

5   MPAS Atmosphere Simulations

We have been conducting global full-physics MPAS-Atmosphere simulations on quasi-uniform meshes with cell-center spacings ranging from 240 km to 3 km. We have also been conducting forecast experiments using variable-resolution meshes for both NWP applications (typically 10-day simulations) and regional climate applications (year-long simulations). Our primary goal in these early experiments is to verify that MPAS-A is producing physically plausible solutions for a given resolution, and to uncover any issues associated with the dynamics solution in the mesh-transition regions on variable-resolution Voronoi meshes.
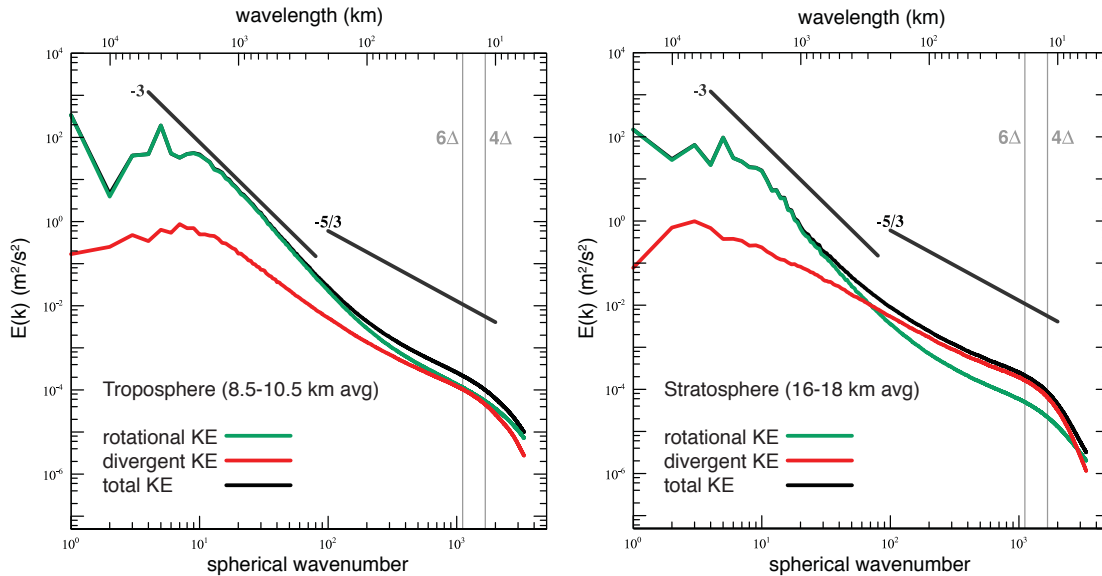
Figure 3: 3km MPAS-A global kinetic energy spectra.

5.1 Kinetic energy spectra

Figure 3 shows the kinetic energy spectra for the troposphere and stratosphere for the 3 km global MPAS-A configuration from a 10-day period (20-30 January 2009) within a 20-day simulation (15 January - 4 February 2009). The mesoscale region is that where the spectra follows an $\sim k^{-5/3}$ behavior, where k is the wavenumber and its exponent is the slope in the log-log plot of the spectrum. Both the troposphere and stratosphere possess a mesoscale region and a transition from the steeper-sloped synoptic scale region. The spectra and its rotational and divergent components are consistent with observations (e.g. Nastrom and Gage, 1985) and other modeling studies (e.g. Hamilton et al, 2008).

We anticipate that the $k^{-5/3}$ behavior should continue to higher wave numbers (shorter wavelengths) as the resolution increases. At approximately $6\Delta h$, however, the spectra begin to steepen again as a result of model filters removing energy at the shorter wavelengths. We refer to the point where the spectra begins to steepen as the *effective resolution* of the model (Skamarock, 2004). The model filters have been adjusted to optimize the effective resolution. In finite-difference and finite-volume formulations, wavelengths less than $\sim 6\Delta h$ have significant spatial discretization error. Because of the downscale energy cascade characteristic of the atmosphere, models require filters to remove energy as they reach their resolution limits to prevent spurious aliasing of energy to the large larger scales.

5.2 Mountain wave examples

Figure 4 shows longitude-height cross sections across the Tibetan Plateau depicting the coordinate surfaces for the 15 km mesh and vertical velocities from a one-day forecast on the 15, 7.5 and 3 km global uniform meshes. The coordinate surface plot (upper left) illustrates the flexibility of the MPAS-A hybrid vertical coordinate (Klemp, 2011). The model top is at $z = 30$ km, and the coordinate surfaces are essentially flat at $z = 20$ km. In the terrain-following portion of the MPAS hybrid coordinate, the shorter-wavelength terrain features are filtered from the mesh more quickly than longer wavelength features thus reducing truncation errors in the horizontal gradients more efficiently than in the traditional terrain-following coordinate formulation.
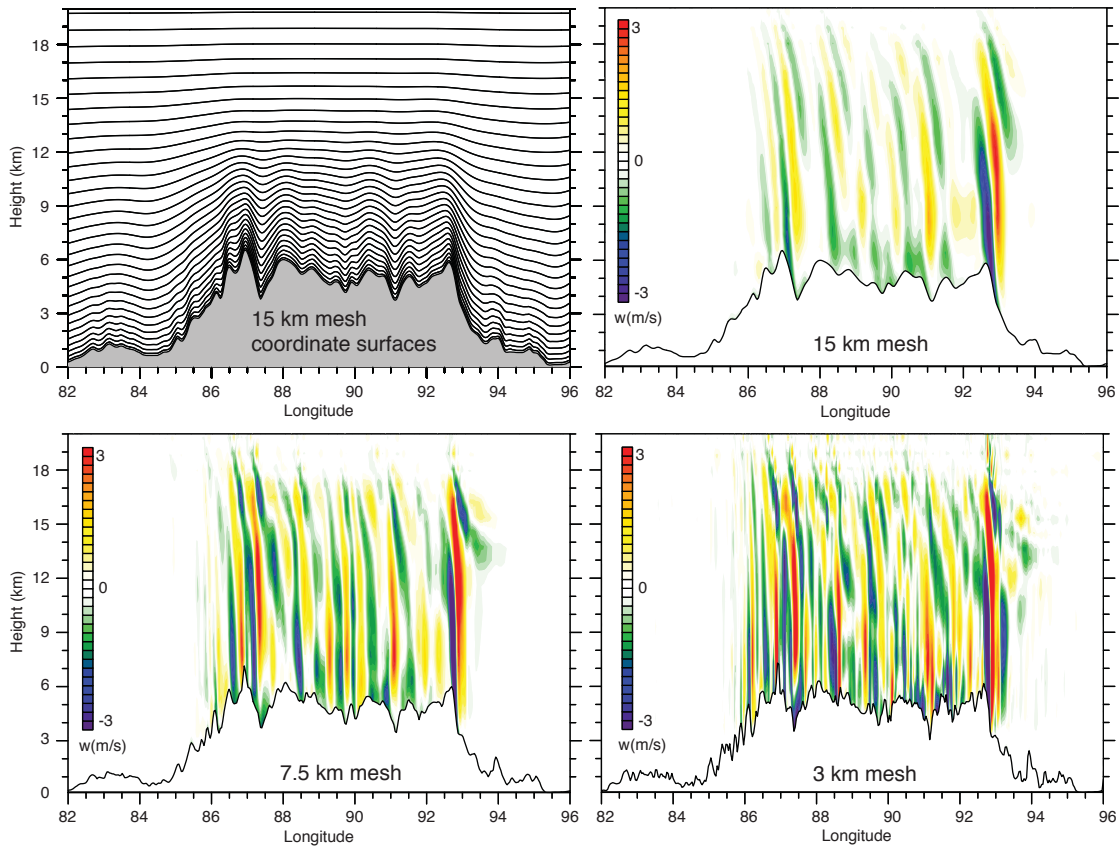
Figure 4: Mountain-wave cross section through the Tibetan Plateau (28 N). 1-Day forecast valid at 0 UTC 16 January 2009. The minimum and maximum vertical velocities are (-3.56, 3.22), (-7.16, 4.92) and (-6.34, 7.10) m/s on the 15, 7.5 and 3 km meshes, respectively. Mount Everest is located at approximately 87 degrees longitude.

Significant westerly flow across the Tibetan Plateau is occurring during this time in the forecast, and mountain waves are evident in the solution on the 15, 7.5 and 3 km meshes. As expected, increased structure is evident on the denser meshes and the maximum and minimum vertical velocities increase with decreasing mesh spacing. A gravity-wave damping layer is used above $z = 22$ km in these forecasts, but these waves are being attenuated at approximately $z = 18$ km due to the presence of a critical layer where the zonal winds are strongly decreasing with height.

5.3 Convection at nonhydrostatic scales

One of the primary reasons to increase resolution into the nonhydrostatic scales is to better resolve topography, as demonstrated in the previous section, and to begin to explicitly resolve convective system structure and evolution. The 3km global MPAS-A configuration does not use a deep convection parameterization - convection is explicitly simulated. Individual deep convective updrafts, however, are rarely observed to have updraft diameters greater than a few kilometers, thus models with mesh spacing above a few hundred meters are considered to be *convection permitting* as opposed to *cloud-resolving* models. Nevertheless, realistic convective system structure and evolution are produced by nonhydrostatic models with convection-permitting mesh densities, particularly in comparison with parameterized-convection simulations. Realistic convective system propagation is observed in the nonhydrostatic simulations that
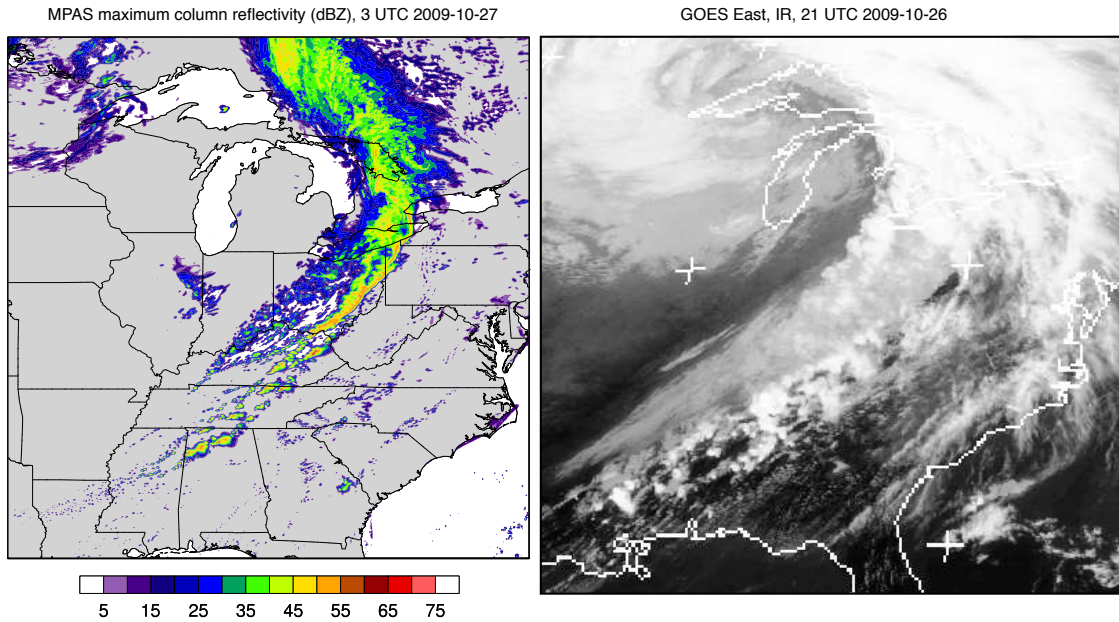
MPAS maximum column reflectivity (dBZ), 3 UTC 2009-10-27   GOES East, IR, 21 UTC 2009-10-26

5   15   25   35   45   55   65   75

Figure 5: 3km global MPAS forecast of radar reflectivity (left, initialized at 0 UTC 23 October 2010) and GOES East IR image.

is often missing from parameterized simulations, and the timing of convection and its precipitation is often better captured.

One important aspect of convection permitting forecasts is their ability to provide information on the type of convection occurring in a given environment. Figure 5 depicts the simulated radar reflectivity from a 3 km global MPAS-A forecast initialized at 0 UTC 23 October 2010. A very strong extratropical cyclone is centered above the Great Lakes region of North America, and its cold front extends down through the Southeast US. In the warm sector ahead (to the east and south) of the cold front, isolated convective cells are evident in the MPAS forecast and in the satellite IR image. Strong isolated convective cells, some of which produced damaging tornadoes, were observed in this region during this time period. While the simulated front lagged the observed front by about 6+ hours in this 4 day 3 h forecast, the nature of the severe convection was well captured. Examination of other convective structures and evolution in this and other convection permitting simulations indicates that MPAS-A reproduces convection with fidelity similar to other regional nonhydrostatic NWP models and research cloud models such as WRF (Skamarock and Klemp, 2008).

5.4 Variable mesh results

We are using the variable-mesh capabilities of MPAS to produce high-resolution regional forecasts within a coarser-resolution global forecasts without the need for traditional one-way and two-way nested grid approaches. We are testing this capability during the 2013 Atlantic hurricane season by producing daily (0 UTC initialization) experimental 10-day MPAS-A forecasts using a uniform 15 km mesh and a variable-resolution 60 - 15 km mesh, where the high-resolution region of the variable resolution mesh covers a significant portion of the Atlantic basin.

An example five-day forecast of 500 hPa relative vorticity from both configurations is depicted in figure 6, and the variable-resolution mesh spacing is also indicated in the figure. These forecast results are typical for these MPAS-A configurations. Several aspects of the comparison are notable. The structure
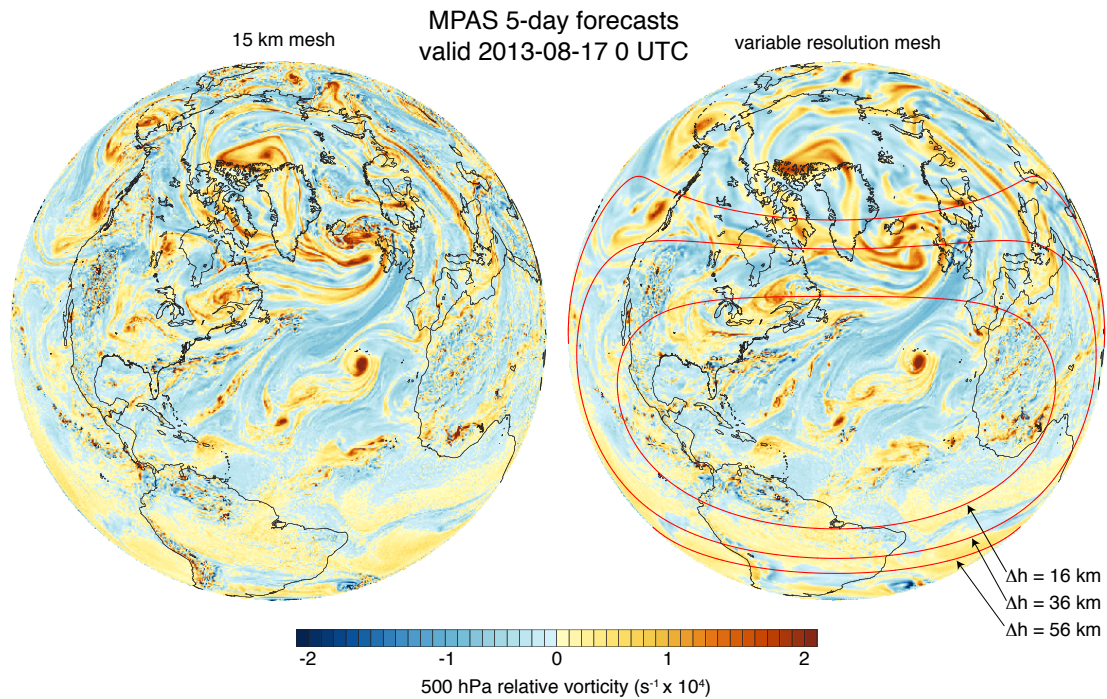
MPAS 5-day forecasts
valid 2013-08-17 0 UTC

15 km mesh

variable resolution mesh

Δh = 16 km
Δh = 36 km
Δh = 56 km

-2   -1   0   1   2
500 hPa relative vorticity (s⁻¹ x 10⁴)

Figure 6: 500 hPa relative vorticity from uniform and variable-resolution mesh forecasts.

in the high resolution region of the variable-resolution mesh is similar to that in the uniform-resolution simulation with regards to the scales resolved on the mesh. For example, Easterly waves are evident in the central Atlantic off the coast of Africa in both simulations, and the structures in the midlatitudes are very similar. In the coarser mesh regions of the variable-resolution mesh forecast (e.g. the polar region in figure 6), the structures are noticeably smoother than those in the higher-resolution uniform mesh forecast, as expected. Importantly, there is a smooth transition of the resolved features in the vorticity field between the coarse and fine-mesh regions and no obvious distortion due to the mesh transition. There are differences in the specific structures between the simulations, as expected in 5-day forecasts using different model configurations. The main results in this comparison using the vertical vorticity fields are also evident in other sensitive model fields, for example vertical velocity.

These preliminary results suggest that the variable-resolution mesh may be viable for use in NWP. We have also performed longer simulations and the results are similar, suggesting that the MPAS variable-resolution meshes may be viable for regional climate applications. Our tests of variable-resolution meshes have been limited to mesh spacings in the hydrostatic regime. We are planning tests of MPAS-A using variable-resolution meshes that span the hydrostatic-nonhydrostatic scales. The development of physics that can accommodate this range of resolutions, particularly the deep convective parameterization, is an important research topic.

References

Davies, T., Cullen, M. J. P., Malcolm, A. J., Mawson, M. H., Staniforth, A., White, A. A., and Wood, N., 2005: A new dynamical core for the Met Offices global and regional modelling of the atmosphere, *Q. J. Roy. Meteorol. Soc.*, **131**, 17591782.

Du Q, M. Gunzburger, L. Ju, 2003: Constrained centroidal Voronoi tessellations on general surfaces. *SIAM J Sci Comput*, **24**,14881506.

Hamilton, K., Takahashi, Y., and Ohfuchi, W., 2008: Mesoscale spectrum of atmospheric motions investigated in a very fine resolution global general circulation model. *J. Geophys. Res.*, **113**, D18110, doi:10.1029/2008JD009785

Hollingsworth, A., P. Kallberg, V. Renner, and D. M. Burridge, 1983: An internal symmetric computational instability. *Quart. J. Roy. Meteor. Soc.*, *109*, 417428.

Hundsdorfer, W. B., B. Koren, M. van Loon, and J. G. Verwer, 1995: A positive finite difference advection scheme. *J. Com- put. Phys.*, **117**, 3546.

Klemp, J. B., 2011: A terrain-following coordinate with smoothed coordinate surfaces. *Mon. Wea. Rev.*, **139**, 21632169.

Klemp. J. B., W. C. Skamarock, and J. Dudhia, 2007: Conservative Split-Explicit Time Integration Methods for the Compressible Nonhydrostatic Equations. *Mon. Wea. Rev.*, **135**, 2897-2913, doi:10.1175/MWR3440.1

Lipscomb W. H., T. D. Ringler, 2005: An incremental remapping transport scheme on a spherical geodesic grid. *Mon. Wea. Rev.* **133**, 23352350.

Lloyd S, 1982: Least squares quantization in PCM. *IEEE Trans Inf Theory*, **28**,129137

Nastrom, G. D., and K. S. Gage, 1985: A climatology of atmospheric wavenumber spectra of wind and temperature observed by commercial aircraft. *J. Atmos. Sci.*, **42**, 950960.

Ničković, M. B. Gavrilov, and I. A. Tosic , 2002: Geostrophic adjustment on hexagonal grids. *Mon. Wea. Rev.*, **130**, 668683.

Ringler, T., M. Petersen, R. L. Higdon, D. Jacobsen, P.W. Jones, M. Maltrud, 2013: A multi-resolution approach to global ocean modeling. *Ocean Modell*. http://dx.doi.org/10.1016/ j.ocemod.2013.04.010

Ringler,T. D, J Thuburn, J.B Klemp, W. C Skamarock, 2009: A unified approach to energy conservation and potential vorticity dynamics for arbitrarily-structured C-grids. *J. Comp. Phys.*, **229**, 3065-3090.

Ringler, T., L. Ju, and M. Gunzburger, 2008: A multiresolution method for climate system modeling: Application of spherical centroidal Voronoi tessellations. *Ocean Dyn.*, **58**, 475498.

Skamarock, W. C, J. B. Klemp, M. G. Duda, L. Fowler, S.-H. Park, and T. D. Ringler, 2012: A Multi-scale Nonhydrostatic Atmospheric Model Using Centroidal Voronoi Tesselations and C-Grid Staggering. *Mon. Wea. Rev.*, **140**, 30903105. doi:10.1175/MWR-D-11-00215.1

Skamarock, W. C. and A. Gassmann, 2011: Conservative Transport Schemes for Spherical Geodesic Grids: High-Order Flux Operators for ODE-Based Time Integration. *Mon. Wea. Rev.*, **139**, 2562-2575, doi:10.1175/MWR-D-10-05056.1

Skamarock, W. C., and J. B. Klemp, 2008: A Time-Split Nonhydrostatic Atmospheric Model for Weather and Forecasting Applications. *J. Comp. Phys.*, **227**, 3465-3485, doi:10.1016/j.jcp.2007.01.037

Skamarock, W. C., 2004: Evaluating Mesoscale NWP Models Using Kinetic Energy Spectra. *Mon. Wea. Rev.*, **132**, 3019-3032.

Thuburn, J., T. D. Ringler, W. C. Skamarock, and J. B. Klemp, 2009: Numerical Representation of Geostrophic Modes on Arbitrarily Structured C-Grids. *J. of Comput. Phys*, **228**, 8321-8335, doi:10.1016/j.jcp.2009.08.006

Wicker, L. J., and W. C. Skamarock, 2002: Time Splitting Methods for Elastic Models Using Forward Time Schemes. *Mon. Wea. Rev.*, **130**, 2088-2097.